

Midinfrared up-conversion imaging under different illumination conditions


Zheng Ge^{1,2,‡}, Zhaoqizhi Han^{1,2,‡}, Yiyang Liu³, Xiaohua Wang^{1,2}, Zhiyuan Zhou^{1,2,*},
Fan Yang,⁴ Yin Hai Li,^{1,2} Yan Li^{1,2}, Li Chen^{1,2}, Wuzhen Li^{1,2}, Sujian Niu^{1,2} and Baosen Shi^{1,2,†}

¹CAS Key Laboratory of Quantum Information, University of Science and Technology of China, Hefei, China

²CAS Center for Excellence in Quantum Information and Quantum Physics, University of Science and Technology of China, Hefei, China

³School of Physical Science and Technology, Lanzhou University, Lanzhou, China

⁴National Key Laboratory of Electromagnetic Space Security, Tianjin, China

 (Received 1 September 2023; revised 30 October 2023; accepted 8 November 2023; published 29 November 2023)

Converting the medium-emitting infrared field to the visible band is an effective image-detection method. We propose a comprehensive theory of image up-conversion under continuous optical pumping, and discuss the relationship between the experimental parameters and imaging field of view, resolution, quantum efficiency, and conversion bandwidth. Theoretical predictions are given based on numerical simulations, which show good agreement with experimental results. In particular, coherent and incoherent light illumination are studied separately and the advantages and disadvantages of their imaging performance are compared and analyzed. This work provides a detailed study of the up-conversion image detection performance of the system, which is of great value in guiding the design of the detection system and bringing it to practical applications.

DOI: [10.1103/PhysRevApplied.20.054060](https://doi.org/10.1103/PhysRevApplied.20.054060)

I. INTRODUCTION

The midinfrared (MIR) spectral region contains the absorption and emission spectral positions of numerous molecules and structures and is often referred to as the chemical fingerprint spectral region for the analysis of the composition of substances [1]. In addition, this band is closely related to the thermal radiation of objects and contains atmospheric communication windows. As a result, MIR spectroscopy has fruitful applications in areas such as biomedicine, [2] environmental monitoring, [3] communications [4], and remote sensing, [5] stimulating extensive research in recent years. However, despite the many advantages of MIR spectroscopy and imaging, the development of detectors in this band is still unsatisfactory, limiting many practical applications. Compared to their visible or near-infrared (NIR) counterparts, MIR detectors suffer from low detection sensitivity, high noise levels, slow response times, and high cost. The detectors based on low band-gap materials, such as mercury cadmium telluride (MCT) and indium antimonide (InSb) have achieved high sensitivity and quantum efficiency, but rely on deep cooling to reduce dark noise, which places additional burden on the applications.

MIR detectors based on nonlinear frequency up-conversion techniques, where the signal light is converted to visible or near-infrared light and then detected using high-performance detectors based on wide band-gap materials (e.g., silicon), offer an effective alternative [6]. This technique is not new and has been relatively well developed for signal detection in the communications band, [7] with the advantages of room-temperature operation and real-time processes. In recent years, up-conversion detection research has begun to expand into the midinfrared band, with studies emerging for single-mode and image detection [8–10]. Waveguide-based up-conversion detectors (UCD) can easily increase power density to achieve high conversion efficiencies due to high power density, [11,12] but the perturbation of the spatial structure of the optical field makes them suitable only for single-point detection situations. Bulk crystals are often used as nonlinear media in up-conversion image detection, and schemes based on ultrafast lasers, [13] cavity enhancement, [14] continuous light with high-power [15], or orbital angular momentum [16] pumping have been reported. Another advantage of UCD over conventional semiconductor-based detectors is the flexible tuning of performance parameters, such as bandwidth, field of view, resolution, and efficiency, which also requires a systematic imaging theory to guide the experimental design. In previous research on this topic, the usual treatment has been to associate the imaging theory of a linear system

*zyzhouphy@ustc.edu.cn

†drshi@ustc.edu.cn

‡These authors contributed equally to this work.

with a nonlinear variation process [17–19]. This type of approach is more convenient in providing resolved results of the final image, but also involves considerable approximations, including neglecting the effect of propagation evolution within the crystal. A better solution would be to combine the analytical derivation with numerical simulations, which can give more accurate predictions of the imaging results. Furthermore, previous research has focused more on the case of coherent light illumination, as lasers have been the mainstay of modern optical research since their inception due to their excellent properties. However, thermal-imaging applications are more oriented towards the spontaneous radiation of the target, and therefore the study of UCD with noncoherent illumination scenarios is of great interest in terms of passive detection. Our work provides a derivation of universally applicable up-conversion imaging results for coherent and incoherent scenarios and shows experimental and theoretical control studies on parameters, such as bandwidth, field of view, resolution, and efficiency.

II. THEORETICAL MODEL AND SIMULATIONS

Up-conversion imaging is based on sum-frequency generation (SFG) in nonlinear crystals, where midinfrared signal light with frequency ω_s is up-converted to ω_{SF} by pump light with frequency ω_p . This process satisfies the law of energy conservation, i.e., $\hbar\omega_{\text{SF}} = \hbar\omega_s + \hbar\omega_p$, where \hbar is Planck's constant. In order to achieve the highest frequency conversion efficiency, quasi-phase-matching (QPM) technique is often used to compensate for the phase mismatch and the poled period is designed such that $\Delta\vec{k} = \vec{k}_s + \vec{k}_p + \vec{k}_\Lambda - \vec{k}_{\text{SF}}$, satisfying the momentum conservation condition, where $|\vec{k}_\Lambda| = 2\pi/\Lambda$ and Λ is the poled period of the crystal. In most nonlinear application scenarios, colinear matching is considered in order to achieve greater beam crossover and thus higher conversion efficiency. However, for the image-conversion scene, the nonlinear process will be a combination of the colinear and noncolinear cases, as the entire signal light field contains the individual components of incidence. By decomposing the phase mismatch wave vectors in the transverse and longitudinal dimensions, universal scalar expressions can be written as

$$\begin{aligned} k_{\text{SF}} \cos \varphi &= k_s \cos \theta + k_p + k_\Lambda \\ k_{\text{SF}} \sin \varphi &= k_s \sin \theta \end{aligned}, \quad (1)$$

where $k_i = 2\pi n_i/\lambda_i$ ($i = p, s, \text{SF}$) are the wave vectors of the pump light, signal light, and sum-frequency light, respectively, which depend on their respective wavelengths λ_j ; the refractive index n_j is given by the Sellmeier equation; and θ and φ denote the angles of the propagation direction of the signal light and the sum-frequency light

relative to the pump light (crystal axial direction), respectively. In a practical up-conversion process, as the wavelength and direction of the pump light are usually constant, the wavelength and angle of incidence of the signal light, which are the independent variables in Eq. (1), determine the corresponding parameters of the up-converted light. Thus, the wavelength-converted bandwidth and the FOV of the system are interrelated, as we will discuss together in the paper. In UCD studies based on single-period crystals, the obtained conversion bandwidths and FOVs are usually very narrow due to the strict phase-matching conditions [20,21]. To overcome these difficulties, feasible attempts include adjusting the crystal temperature, scanning the pump wavelength, rotating the crystal or changing the angle of incidence of the signalling light [22,23]. All of these methods essentially involve adding an adjustable term to Eq. (1) to obtain more group solutions, but have the disadvantage of greatly increasing the complexity of the system and the measurement. Another solution is the use of chirped-poled crystals, which have been used to achieve adiabatic nonlinear conversions with large phase-matching bandwidths, and image conversions with large fields of view have also been demonstrated [24–26]. In general image-detection applications, especially in noncoherent illumination scenarios, the light field collected by the detection system contains numerous frequency and spatial components. Therefore, the use of chirped poled crystals can significantly improve the performance of the image detector due to the much wider phase-matching bandwidth. The blue region in Fig. 1(a) shows the wavelength and incident angle ranges that satisfy the phase-matching condition, and the simulations are based on the chirped crystals in our experiments. The chirped poled structure increases both the wavelength bandwidth and the FOV for all lighting conditions, as explained in more detail in the Supplemental Material [27] (see also Refs. [28–31] therein).

The general case of coherent light illumination is discussed first. There is a certain phase correlation between the points of the illuminated object, and the light maintains spatial and temporal coherence in the process of propagation. The propagation of coherent light illuminating objects in space can be described by the Collins formula, which is known as [32]

$$\begin{aligned} U(x, y) &= \frac{\exp(ikl)}{i\lambda B} \iint U_0(x_0, y_0) \exp\left\{\frac{ik}{2B}[A(x_0^2 + y_0^2) \right. \\ &\quad \left. + D(x^2 + y^2) - 2(xx_0 + yy_0)]\right\} dx_0 dy_0, \end{aligned} \quad (2)$$

where A, B, C, D are the four elements in the transmission matrix; $U_0(x_0, y_0)$ and $U(x, y)$ represent the amplitude distribution of the illuminated object and the amplitude distribution after propagating l on the z axis.

For incoherent illumination, there is no spatial and temporal coherence instead. In the calculation process, the

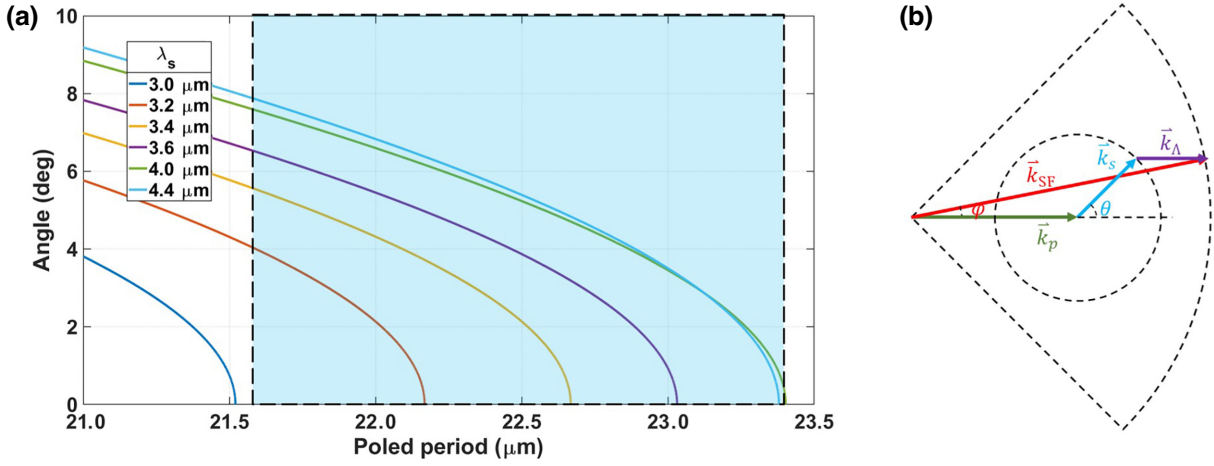


FIG. 1. (a) Theoretical result of the optimized poled period for signal light with different wavelength and incident angle, the blue background area is the region that can meet the phase-matching condition. (b) Phase matching in sum-frequency generation for a certain wavelength of the signal beam. For coherent lighting objects, $\theta = 0$. For incoherent cases, θ can take any value. In chirped crystals, \vec{k}_Λ is variable, which can always find \vec{k}_Λ that meets the phase-matching conditions.

spatial coherence is eliminated by adding random phase fluctuations to the image and adding different propagation directions. The temporal coherence is eliminated by increasing the wavelength range of signal light and averaging multiple calculation results.

The wave equation of the electric vector propagating in the nonlinear crystal can be written as [33–35]

$$\nabla^2 \vec{E}(\omega_n, z) + \mu_0 \omega_n^2 \vec{\epsilon}(\omega_n, z) \cdot \vec{E}(\omega_n, z) = -\mu_0 \omega_n^2 \vec{P}_{\text{NL}}(\omega_n, z). \quad (3)$$

For second-order nonlinear processes, considering the slowly varying amplitude approximation, the scalar complex amplitude of the sum-frequency beam satisfies the differential equation, which gives

$$i2k_{\text{SF}} \frac{\partial E_{\text{SF}}}{\partial z} + \nabla_{\perp}^2 E_{\text{SF}} = -\frac{\omega_{\text{SF}}^2 d_{\text{eff}}}{\epsilon_0 c^2} E_s E_p e^{i\Delta k z}, \quad (4)$$

where $E_i (i = \text{SF}, s, p)$ represents the scalar complex amplitudes of sum-frequency beam, signal beam, and pump beam, respectively; $\Delta k = k_{\text{SF}} - k_s - k_p + 2\pi/\Lambda$ is a phase mismatch during the sum-frequency generation; ϵ_0 and c are the dielectric constant and the speed of light in the vacuum, respectively; $\nabla_{\perp}^2 = \partial^2/\partial x^2 + \partial^2/\partial y^2$ represents the transverse Laplace operator.

The boundary conditions including the amplitude distribution of signal beam, pump beam, and sum-frequency beam at the front of the crystal can be easily obtained. By using the forward difference method to solve the sum-frequency generation process in crystals, the coupled wave

equation can be discretized as

$$E_{\text{SF}}(x, y, z + dz) = E_{\text{SF}}(x, y, z) + \frac{i}{2k_{\text{SF}}} [\nabla_{\perp}^2 E_{\text{SF}}(x, y, z) + \frac{\omega_{\text{SF}}^2 d_{\text{eff}}}{\epsilon_0 c^2} E_s(x, y, z) E_p(x, y, z) e^{i\Delta k z}] dz. \quad (5)$$

With this method, the amplitude distribution of three beams at any position in the crystal can be solved. Finally, the amplitude and intensity distribution of sum-frequency beam after imaging system can be calculated by using the Collins formula again.

III. EXPERIMENT

A. Experimental setup

In the sum-frequency generation, the propagation direction and wave vector of signal light are determined when the object is lighted by coherent beam. The propagation direction of the signal beam in the crystal is single. The lack of signal beam with large angle incidence leads that high-frequency information of its spatial structure cannot be converted, so its detailed imaging effect is not good. For incoherent light, its propagation direction within the crystal is random, and using chirped crystals can convert almost any direction of input beams. The wave-vector direction that can be converted is only limited by the waist of the pump beam, which is generally smaller than the cross-section size of the crystal. Incoherent light illuminating objects can convert more directional wave vectors, so their high-frequency information can be well preserved, achieving clearer imaging effects [see Fig. 1(b)].

A simple diagram of our experimental setup is displayed in Fig. 2. We first generate the incoherent MIR source

using a temperature adjustable soldering pen, and then use a collecting lens to transform the illumination light into a subparallel beam. The U.S. Air Force MIL-STD-150A standard of 1951 (USAF-1951) resolution target is then inserted as the illumination intensity object. The continuous-wave pump beam at the wavelength of 1064 nm comes from a Yb-doped fiber laser amplifier, and is scaled down to a $1/e$ beam waist of 1.5 mm through the lenses L1 ($f = 150$ mm) and L2 ($f = 75$ mm). The type-0 chirped PPLN crystal that we use in our experiment is 40-mm long, with an aperture of 2×3 mm², and its quasi-phase-matching periodic poled period is from 21.6 to 23.4 μm , with an interval of 0.01 μm . The temperature of the PPLN crystal is controlled using a homemade temperature controller with a stability of $\pm 0.002^\circ\text{C}$. Lens L3 ($f = 100$ mm) focuses the MIR image into the PPLN crystal, which together with L4 ($f = 100$ mm) forms the up-converted $4f$ system, while the center of the PPLN crystal lies in the Fourier plane. The output image is cleaned up by using a band-pass 800-nm filter with a full width at half maximum of 40 nm, and then recorded by an sCMOS camera (Dhyana95 V2, Tucsen).

B. Resolution

In the above configuration, the central region of the USAF-1951 resolution card is selected as the intensity object, thus containing more resolution patterns in the field of view. Up-converted images of multiple sets of horizontal and vertical stripes are obtained and the output is shown in Fig. 3(a). Figure 3(c) shows the numerical simulation results for a portion of the region where the up-conversion system reaches its resolution limit. The advantage of this treatment is that it reduces the large computational effort that the oversized image imposes on the numerical simulation, and instead allows smaller step values to be assigned to the stepwise Fourier method, thereby increasing the accuracy of the simulation. The right half of the experimental results agree with the theoretical and simulated results.

For a specific analysis of the imaging resolution, we use the requirements of the Rayleigh criterion as an evaluation metric: $I_{\min} \leq 2I_{\max}/e$. Here I_{\max} is the average maximum intensity value of the line graph, while I_{\min} is the minimum gray value in the dark region between the stripes. Figures 3(b) and 3(d) show the results of the vertical intensity distribution along the yellow dashed line from Fig. 3(a)–(c), where the horizontal orange dashed line is the resolution criterion given by the inequality in the above question. When the valley of the intensity in the streak region falls below the dashed line, this means that the set of patterns is resolvable. Experiments give limit resolution regions for groups 1–5 of the USAF-1951 resolution card, corresponding to a line resolution of 315 μm and an angular resolution of 3.15×10^{-3} in our imaging system. At the same time,

simulations give a line resolution of 300 μm . It is worth noting that the theoretical angular resolution limit given by the system parameters is $R = 1.22\lambda_{\text{MIR}}/D_p$. R is the angular resolution of the system; $D_p = 1.7$ mm is the beam diameter of the pump light inside the crystal; λ_{MIR} is the wavelength of the signal light to be converted, here we take the center wavelength of 4.15 μm within the conversion bandwidth. Substitution of the relevant parameters gives R as 2.98×10^{-3} , which agrees well with our experimental results. This also shows that our UCD system has been fully optimized and that the one only factor limiting better resolution is the diaphragm limitation due to the aperture of the crystal.

In the coherent case, the experiments and simulations are shown in Fig. 3 (e)–(h). Both experiments and simulations give limited resolution regions for groups 1–4 of the USAF-1951 resolution card, corresponding to a line resolution of 353 μm . Compared to coherent cases, incoherent illumination has a better spatial resolution, which validates our theoretical analysis. In addition, due to the wide wavelength range of incoherent light generated by the thermal light source, its spectral range after SFG in the chirped crystal is also wider, which introduces dispersion and reduces spatial resolution.

For imaging experiments, a larger pump-beam waist radius means a larger physical aperture, which improves imaging resolution by ensuring more conversion of the high-frequency components. The thickness of the bulk crystal used in the experiments is 2 mm, which is currently the main factor limiting the optimization of the system resolution. On the other hand, there is a reciprocal limitation between the resolution and the conversion efficiency of the system. This is because the use of long crystals to improve efficiency can lead to image distortion, while a large pump-beam waist results in a significant reduction in power density. Therefore, the most effective way to improve the image resolution is increasing the waist of the pump beam as much as possible under the condition of acceptable conversion efficiency.

C. Conversion efficiency and sensitivity

We also study the relationship between the waist of pump beam and the up-conversion efficiency of the image. The relationship between the up-conversion efficiency and the beam waist and the pump light power is calculated, and the conversion efficiency under different pump optical power is measured experimentally. The results are shown in Fig. 4. Through experiments, it was found that when the waist radius of the beam is 0.75 mm, in the case of coherent light, the up-conversion power efficiency is 0.184%, which is slightly higher than our calculated result 0.122%. It can also be verified through numerical calculations that the up-conversion efficiency is almost inversely proportional to the square of the waist radius of the pump beam. Both

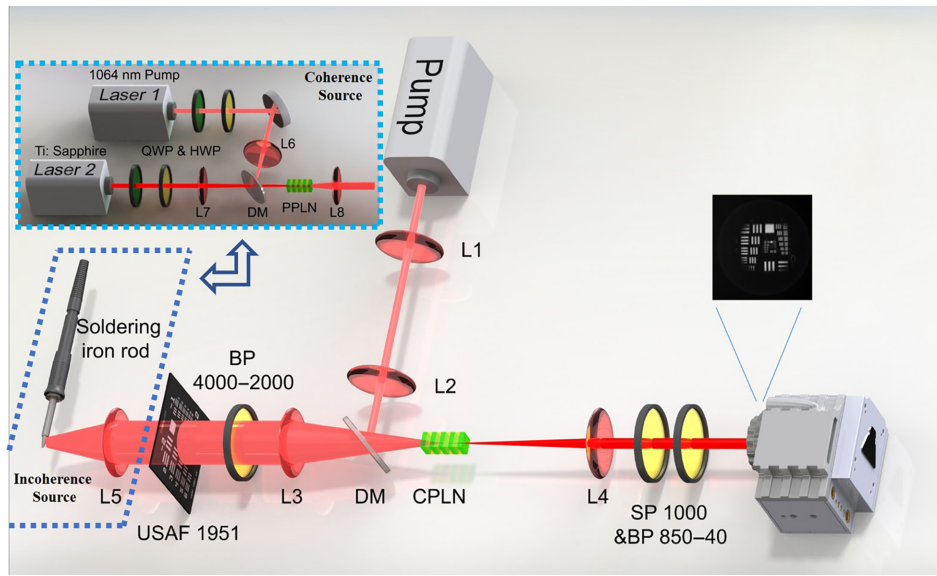


FIG. 2. Schematic diagram of the experimental setup. L terms, the lenses; DM, dichromatic mirror; BP, band-pass filter; PPLN, periodically poled lithium niobate crystal; CPLN, chirped poled lithium niobate crystal.

experiments and simulations give up-conversion power efficiency in incoherent cases 2–3 orders of magnitude lower than coherent illumination conditions. The reason is that incoherent illumination has random phase fluctuations and directions. It is necessary to design crystals, pump parameters and imaging systems for different application scenarios. In addition, the sensitivity of midinfrared up-conversion imaging has also been studied. The intensity of the midinfrared beam before the crystal is 0.813 pW. Under a 45-W pump, the entire area count on the EMCCD camera is about $9.11 \times 10^6 \text{ s}^{-1}$. The imaging results under

the leak illumination are shown in Fig. 5. In conclusion, increasing pump power not only improves conversion efficiency, but also reduces sampling time to achieve more sensitive detection. *Q*-switched lasers can also be used to achieve high efficiency, low noise, and high-sensitivity detection.

D. Field of view

At last, we change the crystal with different poled periods to investigate the field of view, which is mainly limited

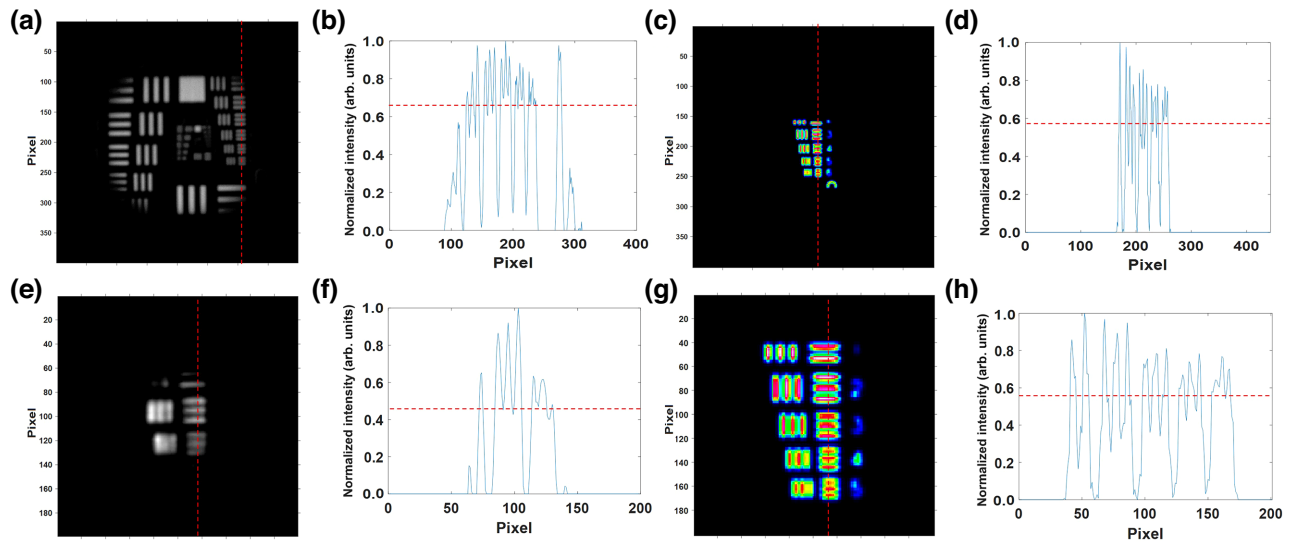


FIG. 3. Experimental incoherent and coherent up-conversion images of the USAF-1951 resolution card. (a)–(d) are incoherent case and (e)–(h) are coherent case. (a),(e) is the up-conversion image and (c),(g) is the numerical simulation results. Line charts (b),(d),(f),(h) correspond to the vertical intensity distributions of images (a),(c),(e),(g), respectively.

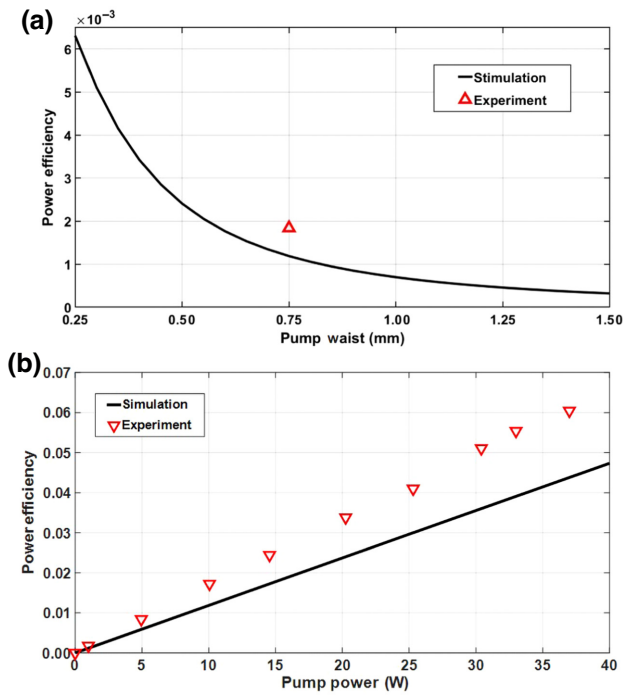


FIG. 4. Simulation and experimental results of up-conversion efficiency. (a) Simulation results of the relationship between power efficiency and beam waist under the 1-W pump. (b) Simulation and experimental results of the relationship between power efficiency and pump power at 0.75-mm beam waist.

by the phase-matching condition in the experiment. We demonstrate that the chirping structure in QPM crystals contributes significantly to the enhancement of the imaging

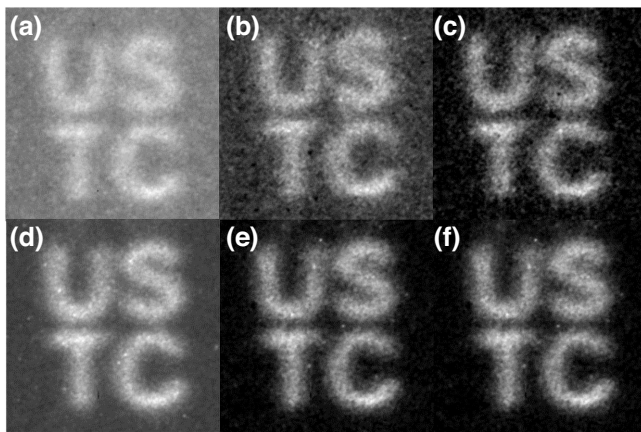


FIG. 5. (a) The noise is mainly composed of electrical noise and pump light noise, with a contrast of 1.74 while the image is not processed. (b) Subtracting the electrical noise result, the main noise is pump light noise, with a contrast of 3.00 (c) Subtracting electrical noise and pump light noise, the contrast is 27.88. (d)–(f) Imaging results of all noise, subtracting electric noise, subtracting electric noise and pump light noise under Q -switched laser pumping. The contrast are 2.85, 53.59, and 65.15, respectively.

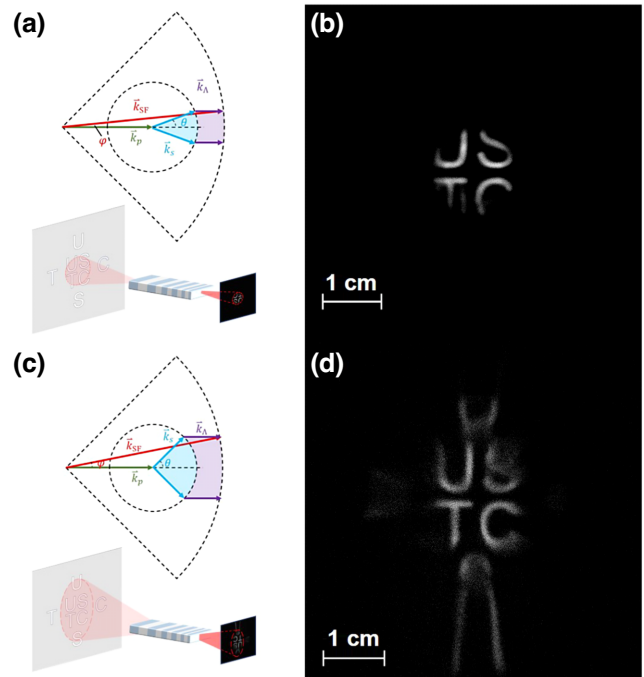
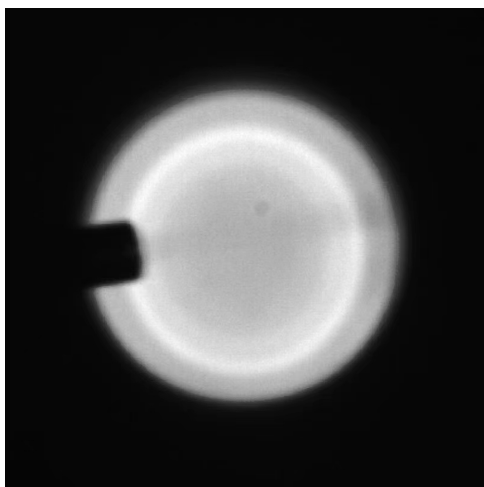


FIG. 6. (a),(c) represent the imaging principles and schematic diagrams of the two different chirped poled crystals, respectively. The purple region represents the valuable range of spatial inverted lattice vectors in the chirped poled crystals, while the blue region represents the valuable range of the angle of signal beam input. The crystal with smaller poled periods has larger spatial inverted lattice vectors to achieve phase matching, thus corresponding to a larger angle of the field of view. (b) The image obtained by using the crystal with chirped poled periods from 23.33 to 23.42 μm . (d) The image obtained by using the crystal with chirped poled period of 21.6 to 23.4 μm .

field of view. In Fig. 6, we show the imaging results of two different chirped-poling crystals under the same illumination conditions with the incoherent signal beam. When a chirped-poling crystal (with periods from 23.33 to 23.42 μm) is used to up-convert the image, it has a small field of view, as shown in Fig. 6(b). This is because the chirping range limits the region of variation of \vec{k}_Λ , i.e., the narrow violet region in Fig. 6(a), and therefore momentum conservation cannot be satisfied for signal light at larger angles of incidence. The full angle of the field of view is 7.7° in this case. Then we chose the chirped crystals with periods from 21.6 to 23.4 μm , and the corresponding up-conversion image has a larger field of view and higher intensity [see in Fig. 6(d)] than the case of the crystal with period from 23.33 to 23.42 μm . In this case, the full width of the imaging area is 29.5 mm and the focal length of lens L1 is 100 mm, so that the full angle of the field of view is 16.8° . These results are consistent with the theoretical results shown in Fig. 1(a). In addition, due to its wide temperature bandwidth, the imaging field of view of chirped



VIDEO 1. CO₂ gas video-rate monitoring. CO₂ has strong absorption at 4.26 μm, which falls within the detection range of our system.

crystals is insensitive to variations in crystal temperature, unlike that of single-period crystals.

E. Application: real-time imaging of CO₂ gas

Our system has the advantages of high efficiency, high sensitivity, and large field of view, so it can perform real-time video imaging of gas distribution and so on. We demonstrated the application of midinfrared up-conversion imaging in gas video-rate monitoring using carbon dioxide gas.

By controlling the flow rate of CO₂, we can change the gas concentration at the nozzle, which can be detected by our real-time imaging system. We can clearly observe that as the ejection speed increases, which means the gas concentration increases and the absorption of midinfrared light is stronger, resulting in a more obvious dark area in the video screenshot. These results are shown in Video 1.

IV. CONCLUSION

In summary, we have investigated a MIR detector based on a frequency up-conversion process and its imaging properties. Midinfrared up-conversion detection in the presence of coherent or incoherent illumination has been achieved using single-period and chirped crystals, respectively. We theoretically analyze the imaging process of UCD, give theoretical predictions of the conversion results by numerical simulations and compare them with experimental results. The effects of experimental parameters on system efficiency, field of view, and resolution are investigated, and the advantages of incoherent imaging over coherent processes are demonstrated. This work provides a systematic fundamental study of this frequency up-conversion-based infrared imaging system, which will help to design and improve UCDs for a variety of application

scenarios. By redesigning crystal parameters and imaging systems, this technology is expected to shine in astronomy, remote sensing, microscopy, and other fields.

ACKNOWLEDGMENTS

Z.G. and Z.Q.Z.H. contribute equally to this work. We would like to acknowledge the support from the National Key Research and Development Program of China (Grants No. 2022YFB3607700, No. 2022YFB3903102), National Natural Science Foundation of China (NSFC) (Grants No. 11934013, No. 92065101, No. 62005068), and Innovation Program for Quantum Science and Technology (Grant No. 2021ZD0301100), and the Space Debris Research Project of China (Grant No. KJSP2020020202). This work is also supported by the Opening Funding of National Key Laboratory of Electromagnetic Space Security. The authors declare no competing interests.

- [1] M. N. Abedin, M. G. Mlynczak, and T. F. Refaat, in *Infrared Remote Sensing and Instrumentation XVIII*, Vol. 7808 (SPIE, San Diego, CA, USA, 2010), p. 191.
- [2] T. P. Wrobel and R. Bhargava, Infrared spectroscopic imaging advances as an analytical technology for biomedical sciences, *Anal. Chem.* **90**, 1444 (2018).
- [3] S. M. Mintenig, I. Int-Veen, M. G. Löder, S. Primpke, and G. Gerds, Identification of microplastic in effluents of waste water treatment plants using focal plane array-based micro-Fourier-transform infrared imaging, *Water Res.* **108**, 365 (2017).
- [4] F. Bellei, A. P. Cartwright, A. N. McCaughan, A. E. Dane, F. Najafi, Q. Zhao, and K. K. Berggren, Free-space-coupled superconducting nanowire single-photon detectors for infrared optical communications, *Opt. Express* **24**, 3248 (2016).
- [5] B. M. Walsh, H. R. Lee, and N. P. Barnes, Mid infrared lasers for remote sensing applications, *J. Lumin.* **169**, 400 (2016).
- [6] A. Barh, P. J. Rodrigo, L. Meng, C. Pedersen, and P. Tidemand-Lichtenberg, Parametric upconversion imaging and its applications, *Adv. Opt. Photonics* **11**, 952 (2019).
- [7] S.-K. Liu, C. Yang, S.-L. Liu, Z.-Y. Zhou, Y. Li, Y.-H. Li, Z.-H. Xu, G.-C. Guo, and B.-S. Shi, Up-conversion imaging processing with field-of-view and edge enhancement, *Phys. Rev. Appl.* **11**, 044013 (2019).
- [8] M. Mancinelli, A. Trenti, S. Piccione, G. Fontana, J. S. Dam, P. Tidemand-Lichtenberg, C. Pedersen, and L. Pavesi, Mid-infrared coincidence measurements on twin photons at room temperature, *Nat. Commun.* **8**, 15184 (2017).
- [9] Y. Wang, K. Huang, J. Fang, M. Yan, E. Wu, and H. Zeng, Mid-infrared single-pixel imaging at the single-photon level, *Nat. Commun.* **14**, 1073 (2023).
- [10] J. Tomko, S. Junaid, P. Tidemand-Lichtenberg, and W. T. Masselink, in *2017 Conference on Lasers and Electro-Optics Europe & European Quantum Electronics Conference (CLEO/Europe-EQEC)* (IEEE, Munich, Germany, 2017), p. 1.

- [11] T. W. Neely, L. Nugent-Glandorf, F. Adler, and S. A. Didams, Broadband mid-infrared frequency upconversion and spectroscopy with an aperiodically poled LiNbO₃ waveguide, *Opt. Lett.* **37**, 4332 (2012).
- [12] K.-D. Buchter, M.-C. Wiegand, H. Herrmann, and W. Sohler, in *CLEO/Europe-EQEC 2009-European Conference on Lasers and Electro-Optics and the European Quantum Electronics Conference* (IEEE, Munich, Germany, 2009), p. 1.
- [13] Q. Zhou, K. Huang, H. Pan, E. Wu, and H. Zeng, Ultrasensitive mid-infrared up-conversion imaging at few-photon level, *Appl. Phys. Lett.* **102**, 241110 (2013).
- [14] J. S. Dam, P. Tidemand-Lichtenberg, and C. Pedersen, Room-temperature mid-infrared single-photon spectral imaging, *Nat. Photonics* **6**, 788 (2012).
- [15] S. Junaid, S. C. Kumar, M. Mathez, M. Hermes, N. Stone, N. Shepherd, M. Ebrahim-Zadeh, P. Tidemand-Lichtenberg, and C. Pedersen, Video-rate, mid-infrared hyperspectral upconversion imaging, *Optica* **6**, 702 (2019).
- [16] X. Qiu, F. Li, W. Zhang, Z. Zhu, and L. Chen, Spiral phase contrast imaging in nonlinear optics: Seeing phase objects using invisible illumination, *Optica* **5**, 208 (2018).
- [17] A. J. Torregrosa, E. Karamehmedović, H. Maestre, M. L. Rico, and J. Capmany, Up-conversion sensing of 2D spatially-modulated infrared information-carrying beams with Si-based cameras, *Sensors* **20**, 3610 (2020).
- [18] C. Pedersen, E. Karamehmedović, J. S. Dam, and P. Tidemand-Lichtenberg, Enhanced 2D-image upconversion using solid-state lasers, *Opt. Express* **17**, 20885 (2009).
- [19] J. S. Dam, C. Pedersen, and P. Tidemand-Lichtenberg, Theory for upconversion of incoherent images, *Opt. Express* **20**, 1475 (2012).
- [20] Z.-Y. Zhou, Y. Li, D.-S. Ding, Y.-K. Jiang, W. Zhang, S. Shi, B.-S. Shi, and G.-C. Guo, Generation of light with controllable spatial patterns via the sum frequency in quasi-phase matching crystals, *Sci. Rep.* **4**, 5650 (2014).
- [21] S. Junaid, J. Tomko, M. P. Semtsiv, J. Kischkat, W. T. Maselink, C. Pedersen, and P. Tidemand-Lichtenberg, Mid-infrared upconversion based hyperspectral imaging, *Opt. Express* **26**, 2203 (2018).
- [22] H. Maestre, A. Torregrosa, C. Fernández-Pousa, and J. Capmany, Ir-to-visible image upconverter under nonlinear crystal thermal gradient operation, *Opt. Express* **26**, 1133 (2018).
- [23] K. Huang, J. Fang, M. Yan, E. Wu, and H. Zeng, Wide-field mid-infrared single-photon upconversion imaging, *Nat. Commun.* **13**, 1077 (2022).
- [24] S. M. Friis and L. Høgstedt, Upconversion-based mid-infrared spectrometer using intra-cavity LiNbO₃ crystals with chirped poling structure, *Opt. Lett.* **44**, 4231 (2019).
- [25] A. Bostani, A. Tehranchi, and R. Kashyap, Super-tunable, broadband up-conversion of a high-power cw laser in an engineered nonlinear crystal, *Sci. Rep.* **7**, 883 (2017).
- [26] A. Barh, M. Tawfiq, B. Sumpf, C. Pedersen, and P. Tidemand-Lichtenberg, Upconversion spectral response tailoring using fanout QPM structures, *Opt. Lett.* **44**, 2847 (2019).
- [27] See Supplemental Material at <http://link.aps.org/supplemental/10.1103/PhysRevApplied.20.054060> for a further analysis of phase-matching conditions and a detailed discussion of the theory of chirped poled crystal imaging, which includes Refs. [28–31].
- [28] M. Born and E. Wolf, *Principles of Optics: Electromagnetic Theory of Propagation, Interference and Diffraction of Light* (Cambridge University Press, Cambridge, UK, 1999).
- [29] J. W. Goodman, *Introduction to Fourier Optics* (W. H. Freeman, New York, NY, USA, 2017).
- [30] G. P. Agrawal, *Nonlinear Fiber Optics* (Academic Press, New York, NY, USA, 2012).
- [31] R. A. Fisher and W. K. Bischel, Numerical studies of the interplay between self-phase modulation and dispersion for intense plane-wave laser pulses, *J. Appl. Phys.* **46**, 4921 (1965).
- [32] H. T. Yura and S. G. Hanson, Optical beam wave propagation through complex optical systems, *JOSA A* **4**, 1931 (1987).
- [33] R. W. Boyd, *Nonlinear Optics, Third Edition* (Academic Press, Orlando, FL, USA, 2008).
- [34] Y.-R. Shen, *Principles of Nonlinear Optics* (Wiley-Interscience, New York, NY, USA, 1984).
- [35] D. A. Kleinman, Nonlinear dielectric polarization in optical media, *Phys. Rev.* **126**, 1977 (1962).